Investigation of chip formation mechanism in ultra-precision diamond turning of silk fibroin film

Zhengjian Wang [a], Xichun Luo [a,*], Jining Sun [b,*], Philipp Seib [c,*], Suttinee Phuagkhaopong [c], Wenlong Chang [a], Jian Gao [a], Amir Mir [a], Andrew Cox [d]

[a] *Centre for Precision Manufacturing, DMEM, University of Strathclyde, Glasgow G1 1XJ, United Kingdom*

[b] *School of Mechanical Engineering, Dalian University of Technology, Dalian 116023, China*

[c] *Strathclyde Institute of Pharmacy & Biomedical Sciences, University of Strathclyde, Glasgow G4 0RE, United Kingdom*

[d] *Contour Fine Tooling Ltd., Stevenage SG1 4QR, United Kingdom*

*Corresponding author: Xichun Luo: xichun.luo@strath.ac.uk; Jining Sun: jining.sun@dlut.edu.cn; Philipp Seib: philipp.seib@strath.ac.uk

Abstract

The importance of silk fibroin particles (size from tens of nanometres to hundreds of microns) as effective drug carriers has been well identified due to their superior mechanical strength, biocompatibility and biodegradability. They are usually fabricated by methods that have difficulties in controlling the size and shape to meet the required functions. In addition, using chemical agents in the fabrication process may result in biological risks and degradation of the fibroin structures. In this study, ultra-precision diamond turning (UPDT) technology is researched as an alternative chemical-free manufacturing approach to generate silk particles in the form of cutting chips with controllable size and shape. The machinability in UPDT of silk fibroin film (hereinafter referred to as silk film) was discussed in terms of specific cutting force and chip morphology. The material removal in UPDT of silk film is taken place in the ductile regime. Experimental results reveal that a rise in the cutting speed could significantly reduce the specific cutting force, while decreasing the depth of cut (DOC) could increase the specific cutting force because of the size effect. Moreover, a sharp point tool using a less than 2.5 μm/rev feed rate is preferred to generate helical silk chips. The formation mechanism of shear bands and serrated chips in UPDT of silk film was investigated with the aid of a finite element and smoothed particle hydrodynamics (FE-SPH) hybrid numerical model with Cowper-Symonds (CS) material equation. The material parameters of silk film were determined for the first time at $p = 7$ and $D = 1140$ s^{-1}. The simulated specific cutting force with this set of material parameters is 49.0% smaller than the measured one. The simulated chip morphology (e.g. shear

band spacing) was also in good agreement with the measured values. The simulation study shows that the shear band formation is done via two joining parts: one part propagates from the cutting edge to the free surface, another part initiates on the free surface and evolves towards the cutting edge. The chip segment is formed by a microcrack propagating from the free surface to the cutting edge. The underlying mechanism of formation of the serrated chip is found to have its roots in the hierarchical structure of silk fibroin.

Keywords: Silk fibroin; Silk particles; Ultra-precision diamond turning; Chip formation mechanism; Serrated chip.

1 Introduction

The *Bombyx mori* (*B. mori*) silkworm silk is a natural composite material mainly composed of two kinds of proteins; 70-80% fibroin and 20-30% sericin [1]. Fibroin fibres have robust mechanical properties [2] and superior cellular compatibility [3]. Therefore, they have been used as surgical sutures and scaffolds for cartilage reconstruction [4]. Not only that, silk particles have shown significant potential as ideal drug carriers for intra-articular [5] and antitumor agents [6]. The evidence shows that they can improve the bioavailability and blood residence time of the drug molecules. Compared with the free drugs, drug-loaded silk particles dramatically increased the pharmacokinetics and cellular uptake [7].

The silk particles are mainly made by chemical processing methods, such as desolvation [8], salting out [9], etc. These production methods require chemical agents that result in contamination to the environment and potential degradation of fibroin structures. Electrospraying [10] and supercritical fluid [11] methods have been extensively investigated as they are easy to scale up. Nevertheless, these two methods require expensive instruments and complicated operations [12]. Some mechanical techniques have also been employed, such as ball milling [13] and bead milling [14]. However, the productivity of these mechanical manufacturing approaches is low, and the dimensional consistency of the fabricated silk particles is often poor. Moreover, most of the existing manufacturing approaches can only make spherical silk particles. In contrast, particles with helical [15], filamentous [16], discoidal [17]

and cylindrical [18] shapes and specified sizes are believed to have better efficacy in terms of targeting and immune clearance for drug delivery than their spherical counterparts [19]. Therefore, the feasibility of using ultra-precision diamond turning (UPDT) to obtain helical silk particles in the form of cutting chips is researched in this paper to seek another highly productive chemical-free manufacturing approach.

To our knowledge, UPDT of silk film has never been attempted before. The silk fibroin has a hierarchical structure in which its beta-sheet crystallites are embedded in the amorphous matrix [20]. At the same time, the crystallites and amorphous matrix have entirely different degrees of strength, stiffness and toughness, which will reduce the machinability of silk fibroin. On the other hand, the investigation of the chip formation mechanism to gain a clear understanding of how the hierarchical structure will influence the cutting morphology is pivotal to the success of future process control to obtain cutting chips with desirable size and shape for drug delivery. Therefore, the machinability and chip formation mechanism in UPDT of silk fibroin become the key research focus of this paper.

However, many challenges exist when making an in-situ experimental observation. Besides, inadequate access to silk fibroin samples restricts the insight into the cutting mechanisms through the experimental route. Thus, the numerical cutting simulation will be carried out in this paper, along with cutting chip characterizations. The conventional finite element (FE) method is laborious to set up correct chip/workpiece separation criteria and handle severe grid distortions. Thus, a finite element and smoothed particle hydrodynamics (FE-SPH) hybrid numerical model will be developed.

It is well known that an accurate constitutive description of the non-linear dynamic behaviour for the machined material is essential for numerical simulation. This description is usually a set of material parameters in analytical material models like Cowper-Symonds (CS) rate-independent model or Johnson-Cook (JC) viscoplasticity model, among others. However, there is not yet an adequate material model with material parameters that can fully describe the damage behaviour in UPDT of silk fibroin. This is another big challenge in the numerical simulation study, which will also be researched.

In this paper, Section 2 concerns the study of the machinability of silk fibroin, including the preparation of silk film samples and conducting UPDT trials. Then, an FE-SPH hybrid orthogonal cutting model will be established in Section 3. In addition, the material parameters in CS rate-independent material law for silk film will be determined, and its accuracy will be verified. Finally, in Section 4, the formation mechanism of shear bands and serrated chips in UPDT of silk film will be revealed for the first time, and its link with the hierarchical structure of the silk fibroin will be established.

2 Machinability of silk film in ultra-precision diamond turning

2.1 Silk fibroin solution preparation

The silk solution is required to be regenerated into films for UPDT, which was made from *B. mori* cocoons based on the reported protocol [21]. In brief, the cocoons were boiled for 1 hour in 25 mM Na_2CO_3. The degummed silk was dissolved in 9.3 M LiBr at 60°C for 3 hours and then dialyzed against water over 48 hours (molecular weight cut-off 3500 Da), yielding a 5-6% w/v silk fibroin solution. The silk solution was diluted to a working concentration of 4% w/v with distilled water.

2.2 Preparation of silk film discs

After an overnight air-dry, silk films were regenerated using 5 ml of silk solutions cast on a 70 mm diameter aluminium mould. This procedure was repeated three times to form thicker semitransparent films. The formed amorphous water-soluble silk films have 15.6 mg of silk fibroin per surface unit (cm^2). The samples were kept in a dry vacuum environment at 25°C and 60% relative humidity to avoid structural changes before UPDT trials. Fig. 1 illustrates two silk film discs.
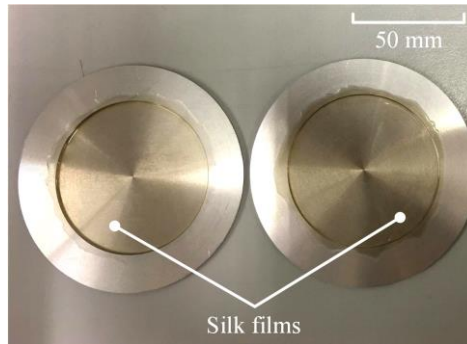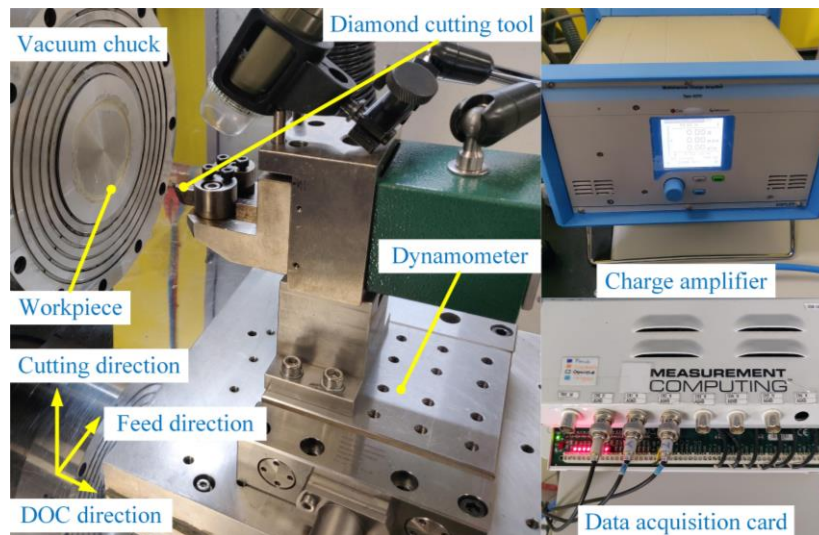
Fig. 1. Silk film samples on aluminium discs.

2.3 Ultra-precision diamond turning experiments

2.3.1 Experimental setup

A couple of UPDT experiments were conducted on a three-axis diamond turning machine. Fig. 2 illustrates the experimental setup.


Fig. 2. Experimental setup.

A silk disc was mounted on a vacuum chuck of the air spindle. A round nose tool with a rake angle of 0˚, a clearance angle of 15° and a nose radius of 0.2 mm was installed on a tool holder to conduct overlapping and non-overlapping cutting trials. Another group of UPDT experiments were performed using a 55° sharp point tool with the same rake and clearance angles as the round nose tool. A three-component dynamometer (9129AA, Kistler) was mounted underneath the tool holder for measurement of cutting force. Before being collected by a data acquisition card (USB-1608HS, Measurement Computing), the force signals were

amplified with a charge amplifier (5070A, Kistler). Furthermore, a scanning electron microscope (SEM) (FEI Quanta 3D FEG) was used to observe the cutting chips.

2.3.2 Cutting conditions and procedure

In UPDT experiments, the dimension relationship between the depth of cut (DOC) and the nose radius of the cutting tool is exaggerated in Fig. 3. A_c is the undeformed chip cross-section area. R_c is the tool nose radius, and d_c is the DOC. The detailed cutting conditions are listed in Table 1.
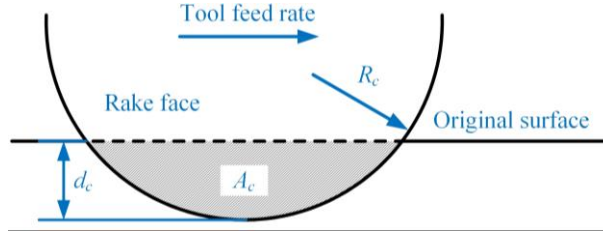
Fig. 3. View normal to the rake face of a round nose tool in UPDT.

Table 1
Cutting conditions

Cutting mode	Cutting speed (m/s)	DOC (μm)	Feed rate (μm/rev)
Non-overlapping	0.027; 0.054; 0.108; 0.27; 0.81; 1.35	1.5; 2	150
Overlapping	1.35	5	1; 2.5; 5
Sharp-point cutting	1.35	5	1; 2.5; 5

Based on the relationship in Fig. 3, while using the round nose tool, it can be expected that when the feed rate is 1, 2.5 and 5 μm/rev, the overlapping cutting will be carried out. Meanwhile, when the feed rate is 150 μm/rev, the experiments will be performed under non-overlapping cutting mode.
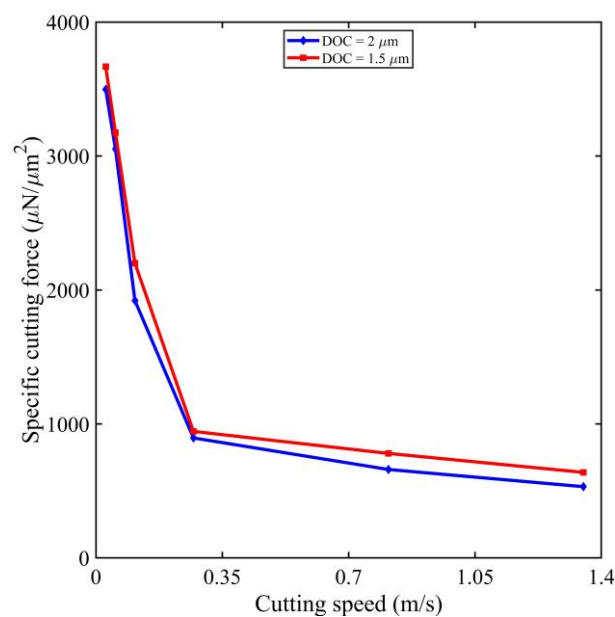
In non-overlapping cutting, the specific cutting force F_s were calculated on the basis of equivalent cutting area to correlate with the simulation results:

$$\begin{cases} F_s = \dfrac{F_c}{A_c} \\ A_c = \dfrac{4\sqrt{2}}{3}\sqrt{R_c d_c{}^3} \end{cases} \quad (1)$$

where F_c is the cutting force measured in the experiments.

2.3.3 Specific cutting force

Fig. 4 illustrates the specific cutting forces with different cutting speeds and depths of cut. It can be demonstrated that the specific cutting forces for 1.5 μm DOC are higher than those for 2 μm, which is due to the size effect of the removed chips. This phenomenon typically occurs when the DOC is approaching the scale of the tool edge radius, and therefore increases the energy dissipation. Specifically, a smaller DOC will trigger a higher strain rate and shear stress. Hence the specific cutting force is increased. The results are consistent with previous UPDT studies on copper [22], aluminium alloy [23] and polymethyl methacrylate [24]. Moreover, the specific cutting force reaches about 3700 μN/μm^2 at the cutting speed of 0.027 m/s, and then decreases dramatically with an increase in the cutting speed. One explanation of this mechanism is that a faster cutting speed will cause more thermal softening [25]. However, the decline rate of the specific cutting force begins to decrease when the cutting speed is over 0.27 m/s. With further increase in cutting speed, a higher amount of heat generated in the primary deformation zone is removed by the cutting chip. Thus the thermal softening is counteracted. In more detail, when the cutting speed is 1.35 m/s, the specific cutting force for 2 and 1.5 μm DOC is 529.6 and 640.2 μN/μm^2, respectively.

Fig. 4. Relationship between specific cutting force, cutting speed and DOC.

2.3.4 Chip morphology

The SEM images of the silk chips formed in non-overlapping cutting experiments with the DOC of 1.5 and 2 μm are illustrated in Fig. 5.
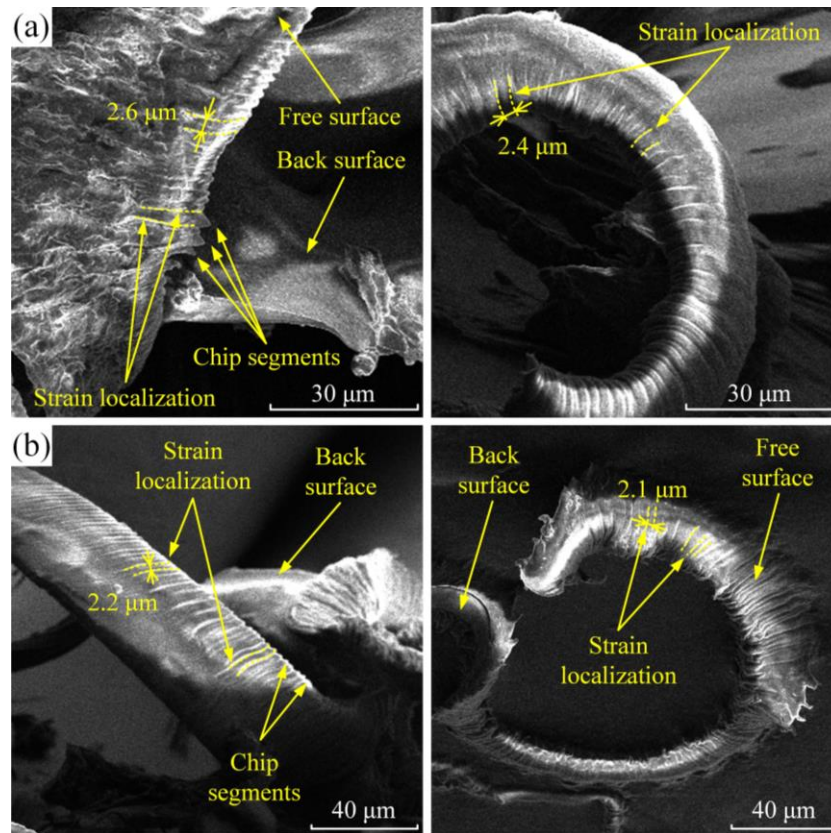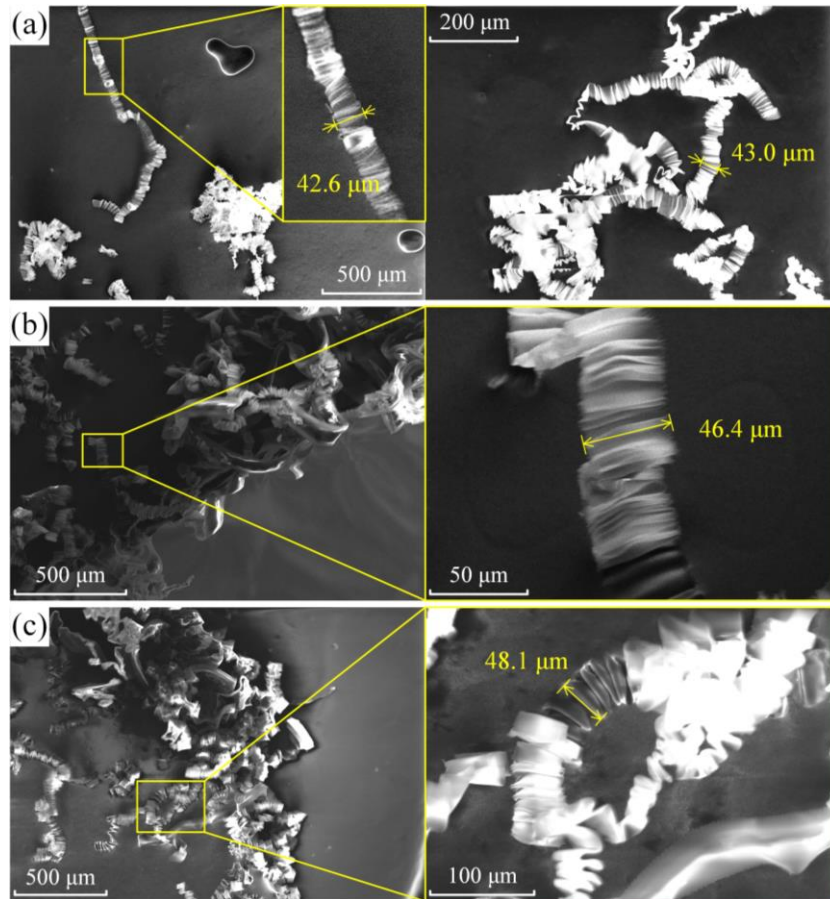

**Fig. 5.** Chip morphology in non-overlapping cutting: (a) DOC = 2 μm; (b) DOC = 1.5 μm.

The serrated chips were obtained under both DOC, where the shear strain localization and chip segmentation can be identified. The back surfaces of the chips are pretty smooth. The chip morphology can be specified using the dimension parameter such as shear band spacing, which will be discussed in Section 3.5 in more detail.

The silk chips generated in overlapping cutting were also collected for SEM measurement, and the results are displayed in Fig. 6. Moreover, Fig. 7 illustrates the SEM images of the silk chips generated by the sharp point tool under the same cutting conditions.

Fig. 6. Chip morphology in overlapping cutting: (a) 1 μm/rev; (b) 2.5 μm/rev; (c) 5 μm/rev.
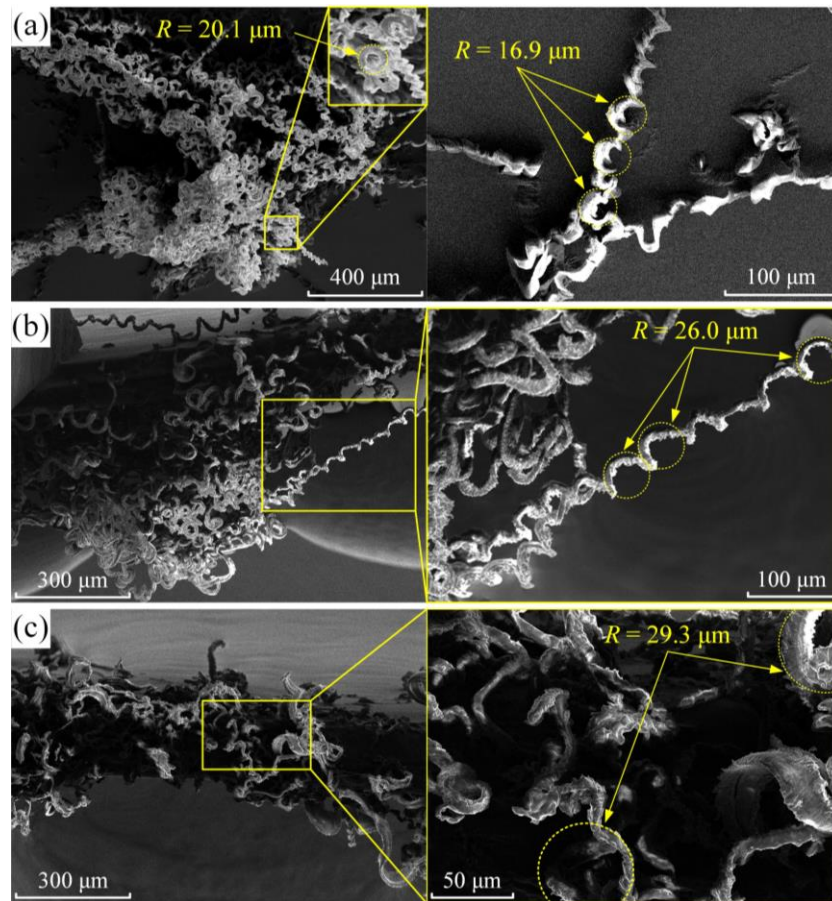
Fig. 7. Chips formed by the sharp point tool: (a) 1 μm/rev; (b) 2.5 μm/rev; (c) 5 μm/rev.

As shown in Fig. 6, the ribbon chips with folds were obtained in overlapping cutting. At the same time, the chip width increases continuously with the increase of feed rate. By contrast, the helical chips with good dimensional consistency are found in Fig. 7(a) and (b). Moreover, Fig. 7(c) illustrates that the chips become snarled as the feed rate grows. This phenomenon shows that the chips develop a larger radius R as the feed rate increases, which is because a higher feed rate will increase the chip cross-section and therefore increase the chip stiffness. Thus, it can be concluded that a sharp point tool under a lower feed rate (i.e. less than 2.5 μm/rev) cutting condition is preferred to generate helical silk chips.

In summary, based on the machinability study of UPDT of silk film regarding the specific cutting force and chip morphology, the ductile mode of cutting of silk film was achieved with the generation of helical silk chips.

3 FE-SPH hybrid modelling

3.1 FE-SPH hybrid scheme

Considerable efforts have been concentrated on the development of numerical cutting models for metals and ceramics [26]. The developed FE framework is mainly based on Lagrangian, Eulerian or Arbitrary Lagrangian-Eulerian (ALE) formulations [27]. Machining processes involve high deformation of workpiece material and hence a major challenge to simulate the chip formation using conventional FE models. For example, Lagrangian formulation has difficulties in handling severe grid distortions. In contrast, no mesh distortion occurs using Eulerian formulation due to the spatially fixed mesh domain. However, Eulerian approach has difficulties in simulating the free surface conditions. A prior assumption of the chip geometry is also required [27]. ALE formulation incorporates the favourable characteristics of Lagrangian and Eulerian techniques, but adaptive remeshing and extra fine mesh size are required. Moreover, the chip shape transition is not accurately predicted due to its dependence on the chip separation model [28].

Conversely, Smoothed Particle Hydrodynamics (SPH) method can easily handle the large-deformation processes, as the workpiece is formed of a group of discrete particles that carry the material properties and state variables. Therefore, the mesh tangling and distortion involving the large strain rate and extreme loading can be avoided. The particle approximation of the function $f(x)$ can be written as [29]:

$$f(\boldsymbol{x}) = \sum_{j=1}^{N} \frac{m_j}{\rho_j} f(\boldsymbol{x_j}) W(\boldsymbol{x} - \boldsymbol{x_j}, h) \tag{2}$$

where m_j, ρ_j and x_j denote the mass, density and location of particle j. Within the effective area, the total number of particles is N. The smoothing length h defines the radius of the effective area in the kernel function W. Outside of this area, the interaction of the central particle with neighbours would be omitted.

Another advantage of SPH is the natural chip/workpiece separation [30]. There is no need to introduce the chip separation criterion (as required in Lagrangian approach) or a pre-defined cutting path to enable the chip/workpiece separation. Unlike Eulerian approach, the free face

generation is entirely manipulated by SPH technique [21]. Unfortunately, SPH technique lacks computational efficiency as compared to FE methods [31].

In this study, a hybrid numerical model based on FE and SPH schemes is adopted to simulate the UPDT process of silk film. The mesh-free SPH technique is used in the large-deformation zone that is subject to extreme strain and strain rate. The rest of the workpiece was modelled using the mesh-based FE method to reduce the computing cost [32]. However, the default SPH formulation cannot manage the accurate particle distributions on the boundaries for the lack of neighbours [33]. Thus, a corrected formulation, named renormalization, was employed in this paper to overcome this problem.

3.2 Material constitutive model

The elastoplastic material model with isotropic/kinematic hardening plasticity was employed to describe the mechanical behaviour of silk film. The stress-strain curve of this material model consists of two linear stages (i.e. elastic stage and plastic stage) [34]:

$$\begin{cases} E = \dfrac{d\sigma}{d\varepsilon}, \sigma < \sigma_y \\ E_{TAN} = \dfrac{d\sigma}{d\varepsilon}, \sigma > \sigma_y \end{cases} \tag{3}$$

where E is the Young's modulus of the work material. σ_y is the yield stress. Based on the available literature [1], the Young's modulus of the regenerated silk fibroin ranges from 1 GPa to 6.5 GPa, while the tensile strength varies from 7 MPa to 100 MPa. E_{TAN} is the tangent modulus which is the slope of the stress-strain curve at the plastic stage. In general, the tangent modulus equals to a few percentages of the material's Young's modulus [35,36].

It can be calculated that UPDT process delivers a high strain rate on the order of 10^6 s^{-1} for a cutting speed higher than 1 m/s [24]. Hence, CS equation which scales the quasi-static yield stress with a factor related to the effective strain rate was adopted [37,38]:

$$\begin{cases} \sigma_{eff} = \left[1 + \left(\dfrac{\dot{\varepsilon_{eff}}}{D} \right)^{1/p} \right] (\sigma_{static} + \beta E_p \varepsilon_{eff}) \\ E_p = E_{TAN} E / (E - E_{TAN}) \end{cases} \tag{4}$$

where σ_{eff} is the effective yield stress and σ_{static} is the quasi-static yield stress. ε_{eff} and $\dot{\varepsilon}_{eff}$ are the effective strain and strain rate, respectively. E_p is the plastic hardening modulus. D and p are a set of material parameters. Parameter p is dimensionless, while parameter D has the same unit as strain rate. Parameter β is the material hardening parameter, which can be used to manipulate isotropic, kinematic or a mix of isotropic and kinematic hardening. In this study, parameter β is set to 0 [34], depending on the large shear deformation in the actual cutting process. The static mechanical properties of silk film are given in Table. 2.

Table 2
Mechanical properties of silk film [39–41]

Parameters	Values
Density (g/cm^3)	1.4
Young's modulus (GPa)	5.2
Poisson's ratio	0.3
Static yield stress (MPa)	70
Tangent modulus (MPa)	172.4

3.3 Orthogonal cutting model

In this work, the non-overlapping UPDT process of silk film is assumed to be an orthogonal cutting process. Moreover, the cutting experiments were carried out at relatively low cutting speeds to reduce the thermal effects on the material. Thus, the temperature effect on the material properties was neglected to simplify the theoretical treatment [42].

A three-dimensional workpiece with the size of 30 μm × 20 μm × 1.6 μm was modelled in an orthogonal cutting framework using LS-PrePost which is a superior pre/post processor that is fulfilled by LS-DYNA. Fig. 8 shows the FE-SPH hybrid numerical model established in this work.
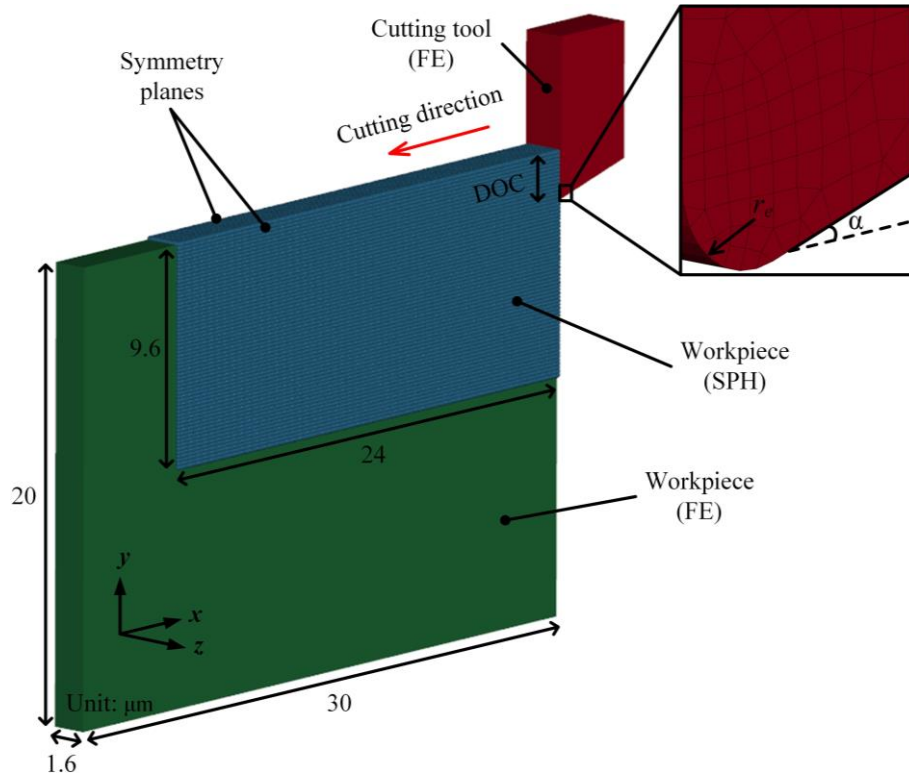
Fig. 8. FE-SPH hybrid numerical model.

The workpiece was split into two domains: one representing the SPH (24 μm × 9.6 μm × 1.6 μm) domain and the rest representing the FE domain. The default eight-node Lagrangian solid elements were used for the FE region of the cutting tool and workpiece. Meanwhile, the renormalized formulation was employed for the SPH domain. After the sensitivity analysis on the particle resolution, the total number of the SPH particles was determined to be 101,321. The minimum mesh size for the continuum FE domain was confirmed to be 0.4 μm. Two symmetry planes were deployed on the front and back faces of the SPH domain to generate ghost particles for maintaining the kernel compactness [43]. In addition, the fixed boundary condition was applied on the left-hand and bottom faces of the workpiece. At the FE-SPH interface, the Lagrangian meshes and SPH particles were coupled by a tied contact formulation. The effectiveness of this treatment was verified via the continuity of von Mises stress along paths through the tied interfaces. The stress changed continuously and smoothly without any large-scale fluctuation.

The tool rake angle was 0°, while the clearance angle α was 15°, which were the same as those in the experiments. The tool edge radius r_e was set at 60 nm, and the meshes near which were

refined for better computing accuracy. The density of the diamond cutting tool is 3.5 g/cm^3 with a Young's modulus of 1050 GPa. The Poisson's ratio of the diamond tool is 0.1. Considering the limited computational resources, the time scaling technique was applied to reduce the computing time, which has been proved as a reasonable assumption [39]. Thus, the cutting speed was set to be 6.75 m/s, which was five times higher than those in actual experiments. The termination time t for all the numerical simulations was 2.2 μs. The Coulomb friction law was introduced to describe the tool/workpiece friction with a coefficient of 0.12 [31].

**3.4 Determination of Cowper-Symonds material parameters**

The CS strain rate hardening model was employed to describe the damage behaviour of silk film under UPDT conditions. There are two material parameters in CS equation, D and p, which artificially increase the yield strength under high strain-rate loading and, therefore, increase the required cutting energy. Considering that there is no material parameter available for silk film yet, the parameter p is preliminarily set to be 5, 7 and 10, based on the values for conventional materials [44–46]. The parameter D ranges from 0.1 to 6500. In this set of the numerical simulations, the DOC was set at 2 μm.

The simulated specific cutting forces with different CS material parameters are shown in Fig. 9. It is easy to conclude that a smaller value of the parameters p can drastically increase the specific cutting force. This is because, based on Eq. (4), a smaller parameter p will lead to a higher scale factor for the yield limit, boosting the critical stress and required cutting energy. However, it does not mean that its value can be decreased unreasonably, as the parameter p significantly influences the chip morphology.
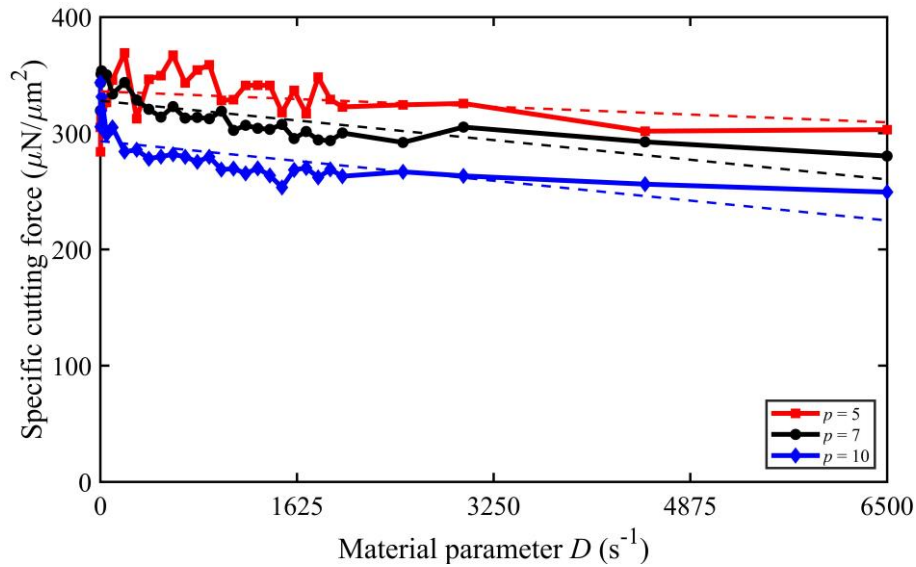
Fig. 9. Simulated specific cutting forces with different material parameters.

The simulation results on chip morphology for various parameter p with fixed parameter D at 1100 s^{-1} are shown in Fig. 10.
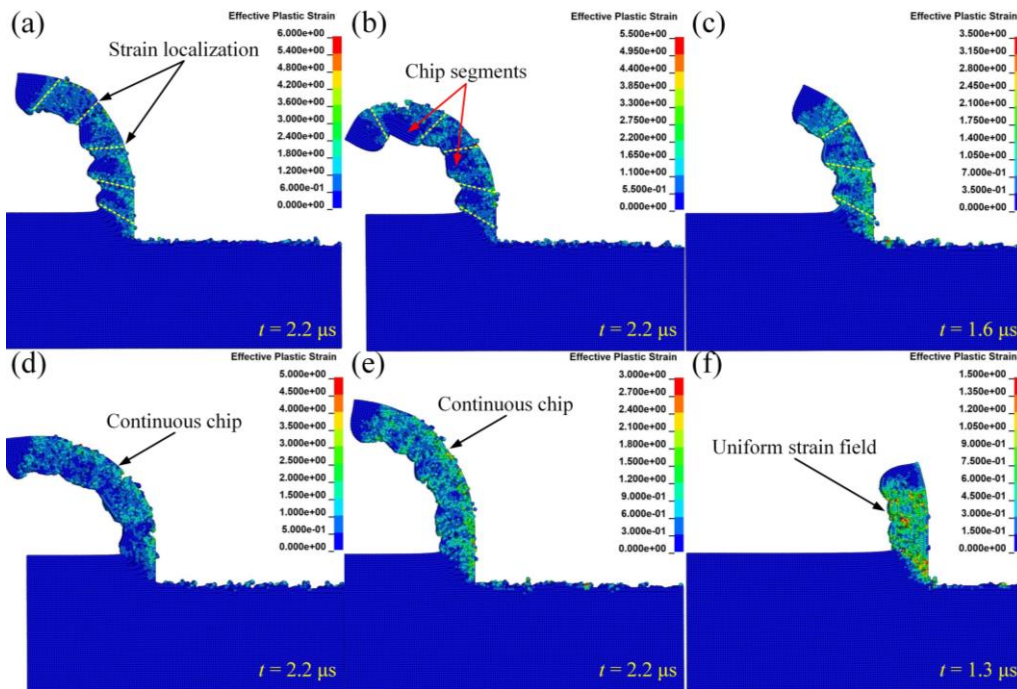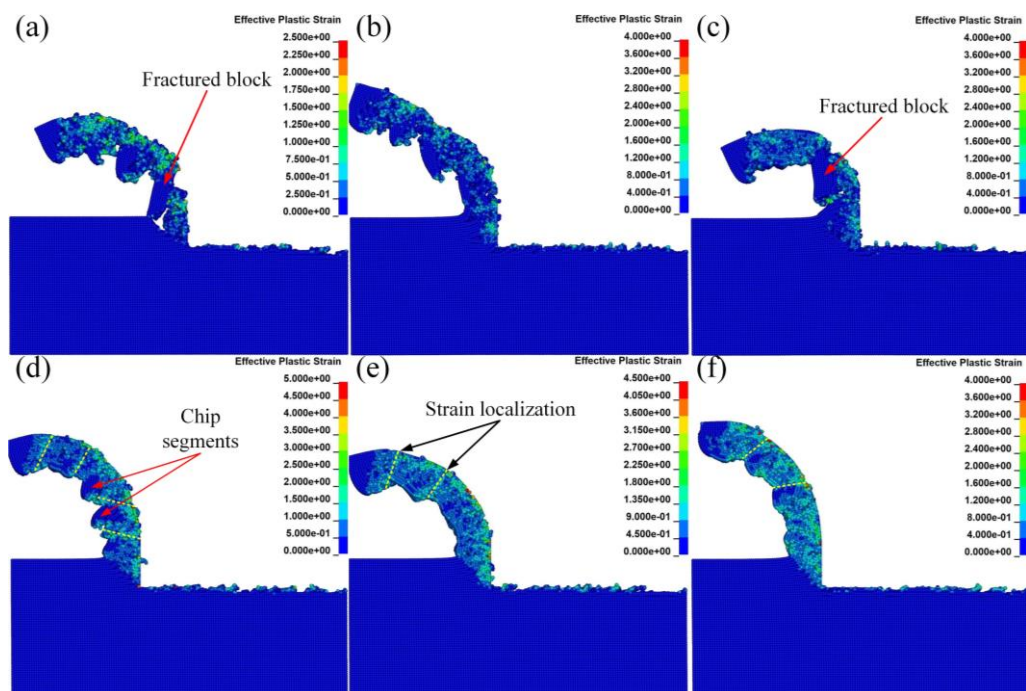

Fig. 10. Simulated chip morphology for (a) $p = 10$; (b) $p = 7$; (c) $p = 6.5$; (d) $p = 6$; (e) $p = 5.5$ and (f) $p = 5$.

When the parameter p is higher than 6.5, the serrated chips with high shear localization and segments are formed, which agrees well with the experiments. However, as the parameter p decreases, the strain field in the chips evolves from shear-localized to be uniform. Moreover,

the numerical instability of the simulation increases significantly. For instance, the numerical simulations collapse without reaching the termination when parameter p equals 6.5 and 5. At the same time, this instability manifests as the drastic fluctuation of the specific cutting force. As shown in Fig. 9, the specific cutting force's fluctuation for the material with $p = 5$ is much larger than those with $p = 7$ and 10. Thus, in this study, parameter p is fixed at 7 to balance the specific cutting force and chip morphology.

The parameter D has a similar impact on the cutting force as parameter p does. Fig. 9 also illustrates that with the increase of parameter D, the specific cutting force decreases. This reduction is owing to a smaller scale factor for the yield strength, although the decline effect of parameter D is not as significant as that of parameter p. But, on the contrary, parameter D exerts a prominent influence on chip shape and material cracking. The simulated chip morphology for various parameter D with parameter p of 7 is illustrated in Fig. 11.

Fig. 11. Simulated chip morphology for (a) $D = 1$ s^{-1}; (b) $D = 10$ s^{-1}; (c) $D = 500$ s^{-1}; (d) $D = 1140$ s^{-1}; (e) $D = 2000$ s^{-1} and (f) $D = 4500$ s^{-1}.

Fractured block chips are generated when parameter D is relatively low (e.g. less than 500 s^{-1}), as a decrease in parameter D increases the brittleness of the material and accelerates its cracking process. This phenomenon is contrary to the experimental results. As illustrated in Fig. 5, the

serrated chips with shear localization were obtained in cutting trials. Furthermore, parameter D also affects the chip morphology and shear band spacing, as the shear localization phenomenon is weakened by increasing parameter D.

In summary, the material with $p = 7$ and $D = 1140$ s^{-1} can obtain a good prediction in terms of the shear band spacing and specific cutting force. Therefore, the CS material parameters for silk film are characterized. The effectiveness and accuracy of the FE-SPH hybrid model along with the determined CS material parameters will be discussed in the following section.

3.5 Model evaluation and verification

The simulated chip morphology with and without CS material model are compared in Fig. 12 to evaluate and verify the model established in this paper.
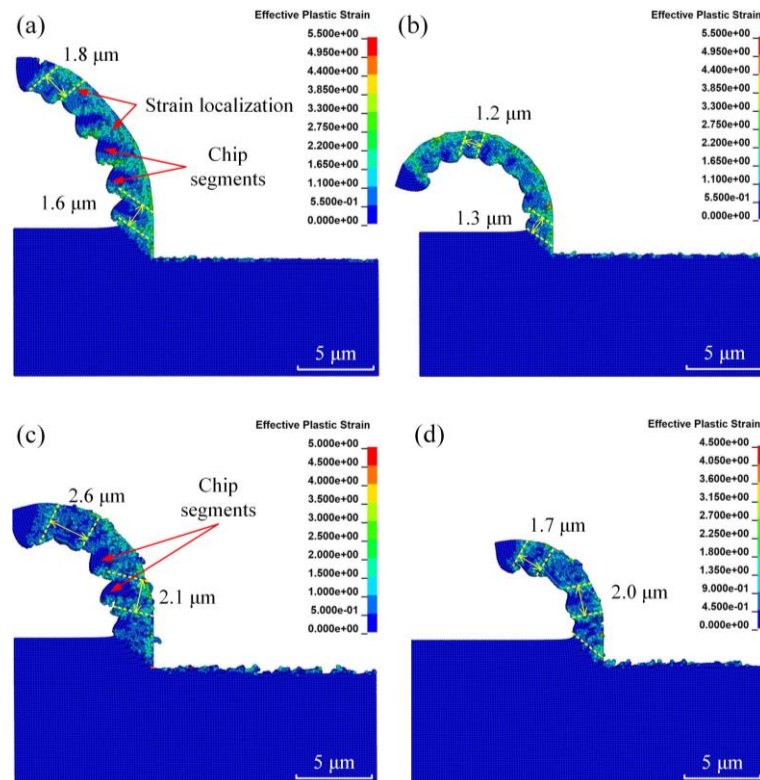

Fig. 12. Simulated chip morphology: (a) without CS model (DOC = 2 μm); (b) without CS model (DOC = 1.5 μm); (c) $p = 7$; $D = 1140$ s^{-1} (DOC = 2 μm); (d) $p = 7$; $D = 1140$ s^{-1} (DOC = 1.5 μm).

The shear strain localization and chip segmentation on the free surfaces can be identified in all the simulated chips, which is consistent with the experimental results in Fig. 5. The approximate

shear band spacing in experiments with a DOC of 2 μm is 2.4 μm. In addition, the measured shear band spacing with a DOC of 1.5 μm is about 2.1 μm. However, the simulated shear band spacing without introducing CS model is much smaller than that in the experiments. In such case, as shown in Fig. 12(a) and (b), the shear band spacings for a DOC of 2 μm and 1.5 μm are generally less than 1.8 μm and 1.3 μm, respectively. In contrast, with the aid of CS model ($p = 7$; $D = 1140$ s^{-1}), the shear band spacings increase significantly. They approach higher than 2.1 μm and 1.7 μm for a DOC of 2 μm and 1.5 μm, respectively, which is in good agreement with the measured results.

After the introduction of CS model, a better estimation of the specific cutting force is achieved as well. Fig. 13 compares the simulated and measured specific cutting forces.
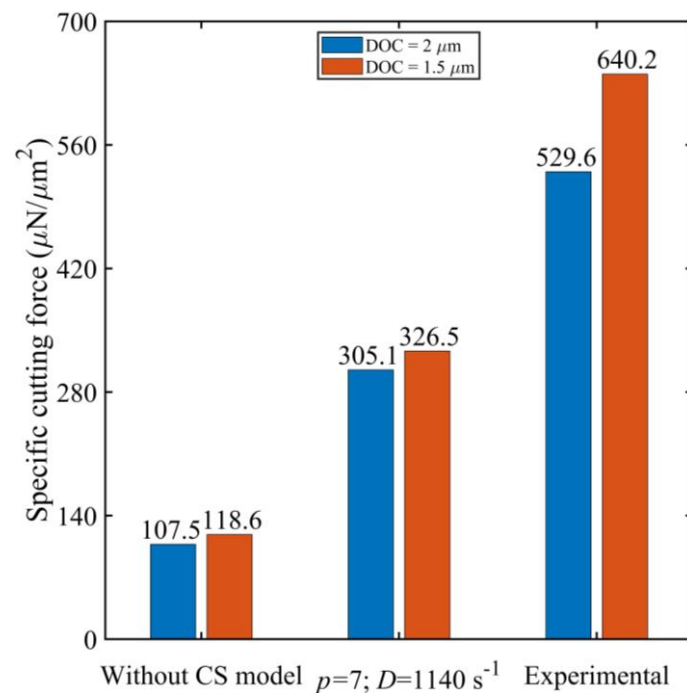
Fig. 13. Simulated specific cutting forces comparisons.

For instance, when the DOC is 2 μm, the specific cutting force obtained from the numerical simulation without considering the strain rate effect is 107.5 μN/μm^2, which is only one-fifth of the experimental result. A similar underestimation can be observed when the DOC is 1.5 μm. However, with the aid of the determined CS parameters, the specific cutting force with the DOC of 2 μm reaches 305.1 μN/μm^2, which is 57.6% of the experimental value. Moreover, when the DOC is 1.5 μm, the specific cutting force obtained from the numerical simulation for material

with $p = 7$ and $D = 1140$ s^{-1} is 326.5 μN/μm^2, which is 51.0% of the measured result. The estimation difference is due to that only strain-rate hardening is included in the material constitutive model without considering the strain and thermal effects. Nevertheless, the effectiveness of the established FE-SPH hybrid model and the accuracy of the determined CS material parameters for silk film are verified considering the good prediction regarding the specific cutting force and chip morphology.

4 Serrated chip formation mechanism

4.1 von Mises stress and plastic strain

As an equivalent stress, von Mises stress can clearly describe the changing of the inner stress of silk film during the chip formation process. The simulated evolution of von Mises stress and distribution of the effective plastic strain with the aid of CS model ($p = 7$; $D = 1140$ s^{-1}) is shown in Fig. 14 and 15, respectively. The cutting speed and DOC were set at 6.75 m/s and 2 μm.
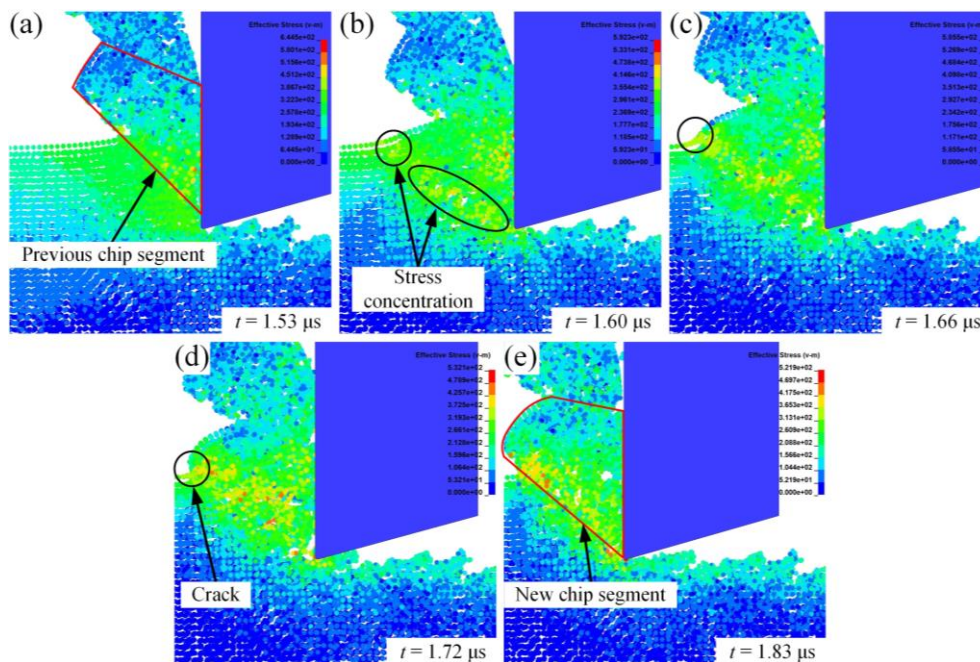
Fig. 14. Evolution of von Mises stress (unit: MPa): (a) the beginning of a new formation cycle of the chip segment; (b) the von Mises stress concentrates at the tool tip and on the free surface; (c) the crack starts to initiate on the free surface; (d) the crack grows; (e) a new chip segment is formed.
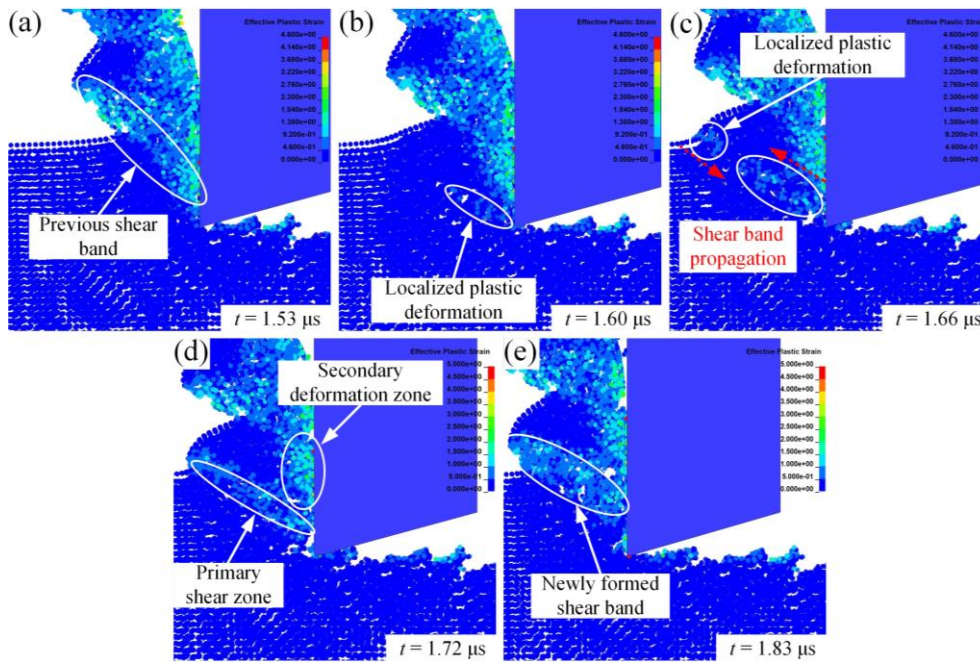
**Fig. 15.** Evolution of effective plastic strain: (a) the start of a new cycle of shear band formation; (b) formation of the first part of the shear band; (c) formation of the second part of the shear band and shear band propagation; (d) recognition of the primary and secondary deformation zones; (e) a new shear band is formed.

Fig. 14(a) and 15(a) show the initiation of a new shear band after a previous shear band is entirely formed. Fig. 14(b) illustrates that the von Mises stress concentrates at the tool tip and free surface. In addition, the stress contour implies that the concentration of von Mises stress at the tool tip is higher than that on the free surface. When the effective stress exceeds the elastic limit of the silk film, it causes plastic deformation to release the stress. As shown in Fig. 15(b), the localized plastic deformation in the form of a shear band initiates in front of the tool tip first and above the cutting edge. At the same time, the maximum effective stress decreases continuously. Afterwards, another plastic deformation zone forms on the free surface in a relatively small area, as illustrated in Fig. 15(c). With the advance of the cutting tool, the first part of the shear band evolves from the cutting edge towards the free surface, whereas the second part propagates from the free surface to the cutting edge. Under the collective efforts of two independent shear bands, an integrated and new shear band is formed by their conjunction.

Moreover, the chip segments are marked in Fig. 14(a) and (e). A crack on the free surface initiates after the material exceeds the strain limit, and it propagates towards the tool tip. The chip segment is, therefore, generated. The primary shear zone and secondary deformation zone can also be identified in Fig. 15(d) due to the severe material shearing and tool-chip friction.

4.2 Underlying mechanism

The formation mechanism of serrated chips in UPDT of silk film has its roots in the unique hierarchical structure. Fig. 16 illustrates that silk fibroin is a protein material that consists of two primary phases; the beta-sheet crystallite and the amorphous matrix. The beta-sheet domain is composed of sandwich-structured assemblies connected by interstrand hydrogen bonds (H-bonds) that primarily control the mechanical properties of the silk fibroin [47].
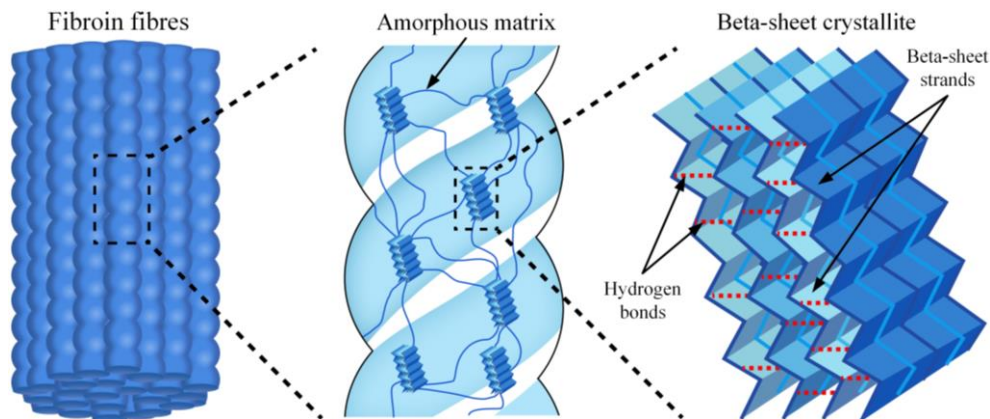
Fig. 16. The hierarchical structure of silk fibroin.

In analogy to the initiation and propagation of dislocation in ductile metals, the breaking of H-bonds has been recognised as the basic mechanism for failure in silk fibroin [48]. After the initial rupture of H-bonds under high shear deformation, the stick-slip motion occurs as the beta-sheet strand slides [49]. This fracture mechanism has been verified with the aid of experiments and molecular dynamics simulations [20,50]. Therefore, the increasing slide motions enable the localized deformation and formation of the shear bands, which results in the serrated chips.

In addition, the oscillation of the specific cutting force and the contour of the effective plastic strain in the simulation of the cutting process are illustrated in Fig. 17. The simulation conditions are the same as those in Section 4.1.
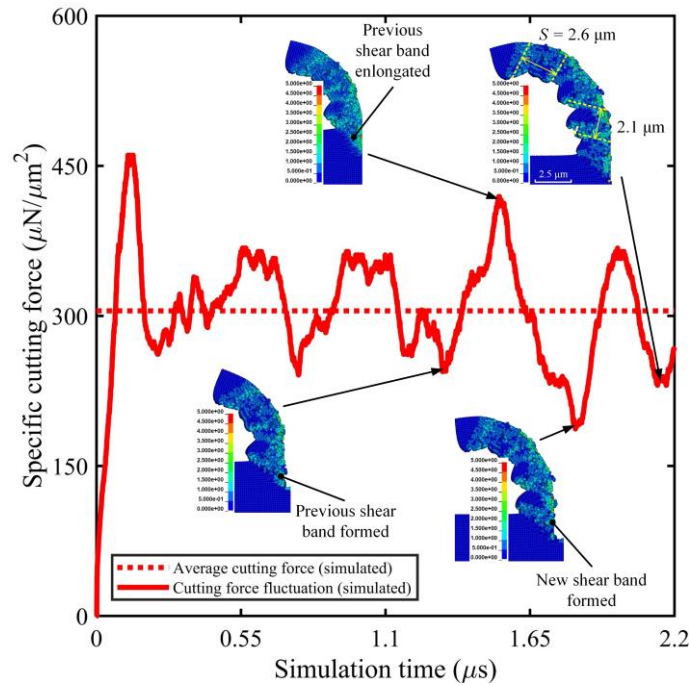
Fig. 17. The simulated specific cutting force oscillation under a cutting speed of 6.75 m/s and a DOC of 2 μm.

The shear deformation is extremely high in UPDT process of silk film. Thus, under the high shear strain in the primary shear zone, the increasing number of rupture H-bonds enables interfaces between beta-strands to become slip planes, followed by the interstrand slip motion. Subsequently, accompanying the formation of shear bands, the accumulated slip motions develop into shear-governed plastic deformation, which is the principal cause of the formation of serrated chips. After the formation of the previous shear band, the material still undergoes heavy shearing along the narrow primary shear zone, in which the shear band is continuously elongated above the cutting edge. At the same time, the von Mises stress is accumulated around the tool tip, and the elastic energy is stored. Thus, the cutting force increases and reaches its peak value. Accompanying the emergence and propagation of a new shear band, the localized plastic deformation releases the accumulated elastic energy. Simultaneously, the cutting force decreases gradually and reaches its lowest value in a single chip formation cycle until the new shear band is completely formed. Afterwards, a new formation cycle for the next shear band and chip segment starts.

In this work, the simulation can only run 2.2 μs due to the limitation of computational power. As the sampling frequency of the data acquisition card for the dynamometer is 250 kHz, it is impossible to compare the oscillation of the measured and simulated specific cutting forces. Nevertheless, the good consistency of the chip morphology obtained in experiments and simulations regarding the shear band spacing S, as illustrated in Fig. 5 and 17, can support the proposed serrated chip formation mechanism. Moreover, as shown in Fig. 18, the lamellar structures on the free surface of the chip generated in the non-overlapping cutting experiment provide another evidence of shear localization.
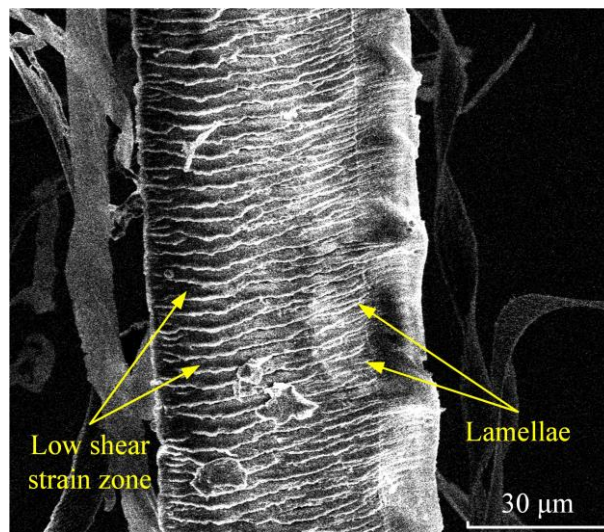
Fig. 18. Lamellae on the free surface of a silk chip generated under a cutting speed of 1.35 m/s and a DOC of 2 μm.

Two areas can be distinguished in SEM images of the chip: (a) a strain localized area (b) a low deformed area. This plastic field distribution is correctly predicted using the FE-SPH hybrid numerical model established in this paper.

5 Conclusions

This study investigated the machinability and serrated chip formation mechanism in UPDT of silk film through cutting experiments and the FE-SPH hybrid numerical simulations. The effectiveness of the established cutting model and the accuracy of the characterized CS material parameters for silk film are verified in terms of the specific cutting force and chip morphology. Helical chips with tunable radius were successfully fabricated using the sharp point tool with a

feed rate of less than 2.5 μm/rev, making it possible to exert size and shape control over the silk chips for potential biomedical applications. The conclusions can be drawn as follows:

(1) An increase in the cutting speed could reduce the specific cutting force as a result of material softening. Meanwhile, a reduction in the DOC could increase the specific cutting force due to the size effect.

(2) The CS material parameters for silk film were preliminarily determined to be $p = 7$; $D = 1140$ s^{-1}. The strain rate sensitivity of the silk fibroin was revealed from a diamond turning aspect. A dramatic increase of the predicted specific cutting force can be observed after introducing CS strain rate model. The specific cutting force for material with $p = 7$; $D = 1140$ s^{-1} is three times higher than those without considering the strain rate effect, despite a 49.0% underestimation compared with the experimental value. Nevertheless, compared with the experiments, a good prediction accuracy regarding the chip morphology was also achieved with this set of material parameters.

(3) The proposed FE-SPH hybrid numerical model is able to reveal the formation mechanism of the serrated chip in UPDT of silk film. The shear band formation is done via the conjunction of two parts: one part propagates from the cutting edge to the free surface, another part initiates on the free surface and propagates towards the cutting edge. Furthermore, the chip segment is formed by the propagation of a microcrack from the free surface to the tool tip.

(4) The serrated chip formation mechanism derives from the hierarchical structure of the silk fibroin. Under the high shear strain in UPDT, the increasing number of rupture H-bonds enables the interfaces between beta-strands to become slip planes. The accumulated interstrand slip motions further develop into shear bands, which is the dominating cause for the formation of serrated chips.

Declaration of competing interests

The authors declared that they have no conflicts of interest in this work.

Acknowledgements

Availability of data and materials

The data underpinning this publication is openly available from the University of Strathclyde Knowledge Base.

References

[1]   Colomban P, Jauzein V. Silk: Fibers, films, and composites—types, processing, structure, and mechanics. Handb. Prop. Text. Tech. Fibres, Elsevier; 2018, p. 137–83. https://doi.org/10.1016/B978-0-08-101272-7.00005-5.

[2]   Koh LD, Cheng Y, Teng CP, Khin YW, Loh XJ, Tee SY, et al. Structures, mechanical properties and applications of silk fibroin materials. Prog Polym Sci 2015;46:86–110. https://doi.org/10.1016/j.progpolymsci.2015.02.001.

[3]   Cao Y, Wang B. Biodegradation of silk biomaterials. Int J Mol Sci 2009;10:1514–24. https://doi.org/10.3390/ijms10041514.

[4]   Kapoor S, Kundu SC. Silk protein-based hydrogels: Promising advanced materials for biomedical applications. Acta Biomater 2016;31:17–32. https://doi.org/10.1016/j.actbio.2015.11.034.

[5]   Bessa PC, Balmayor ER, Azevedo HS, Nürnberger S, Casal M, van Griensven M, et al. Silk fibroin microparticles as carriers for delivery of human recombinant BMPs. Physical characterization and drug release. J Tissue Eng Regen Med 2010;4:349–55. https://doi.org/10.1002/term.245.

[6]   Philipp Seib F. Silk nanoparticles—an emerging anticancer nanomedicine. AIMS Bioeng 2017;4:239–58. https://doi.org/10.3934/bioeng.2017.2.239.

[7]   Tian Y, Jiang X, Chen X, Shao Z, Yang W. Doxorubicin-loaded magnetic silk fibroin nanoparticles for targeted therapy of multidrug-resistant cancer. Adv Mater 2014;26:7393–8. https://doi.org/10.1002/adma.201403562.

[8]   Pham DT, Saelim N, Tiyaboonchai W. Alpha mangostin loaded crosslinked silk
        fibroin-based nanoparticles for cancer chemotherapy. Colloids Surfaces B
        Biointerfaces 2019;181:705–13.
        https://doi.org/https://doi.org/10.1016/j.colsurfb.2019.06.011.

[9]   Lammel AS, Hu X, Park S-H, Kaplan DL, Scheibel TR. Controlling silk fibroin
        particle features for drug delivery. Biomaterials 2010;31:4583–91.
        https://doi.org/https://doi.org/10.1016/j.biomaterials.2010.02.024.

[10]   Qu J, Liu Y, Yu Y, Li J, Luo J, Li M. Silk fibroin nanoparticles prepared by
        electrospray as controlled release carriers of cisplatin. Mater Sci Eng C Mater Biol
        Appl 2014;44:166–74. https://doi.org/10.1016/j.msec.2014.08.034.

[11]   Xie M, Fan D, Li Y, He X, Chen X, Chen Y, et al. Supercritical carbon dioxide-
        developed silk fibroin nanoplatform for smart colon cancer therapy. Int J
        Nanomedicine 2017;12:7751–61. https://doi.org/10.2147/IJN.S145012.

[12]   Pham DT, Tiyaboonchai W. Fibroin nanoparticles: a promising drug delivery system.
        Drug Deliv 2020;27:431–48. https://doi.org/10.1080/10717544.2020.1736208.

[13]   Rajkhowa R, Wang L, Wang X. Ultra-fine silk powder preparation through rotary and
        ball milling. Powder Technol 2008;185:87–95.
        https://doi.org/10.1016/j.powtec.2008.01.005.

[14]   Kazemimostaghim M, Rajkhowa R, Tsuzuki T, Wang X. Production of submicron silk
        particles by milling. Powder Technol 2013;241:230–5.
        https://doi.org/10.1016/j.powtec.2013.03.004.

[15]   Zhong S, Cui H, Chen Z, Wooley KL, Pochan DJ. Helix self-assembly through the
        coiling of cylindrical micelles. Soft Matter 2007;4:90–3.
        https://doi.org/10.1039/b715459c.

[16]   Petros RA, Desimone JM. Strategies in the design of nanoparticles for therapeutic
        applications. Nat Rev Drug Discov 2010;9:615–27. https://doi.org/10.1038/nrd2591.

[17]   Muro S, Garnacho C, Champion JA, Leferovich J, Gajewski C, Schuchman EH, et al.
        Control of endothelial targeting and intracellular delivery of therapeutic enzymes by

modulating the size and shape of ICAM-1-targeted carriers. Mol Ther 2008;16:1450–8. https://doi.org/10.1038/mt.2008.127.

[18]   Decuzzi P, Godin B, Tanaka T, Lee SY, Chiappini C, Liu X, et al. Size and shape effects in the biodistribution of intravascularly injected particles. J Control Release 2010;141:320–7. https://doi.org/10.1016/j.jconrel.2009.10.014.

[19]   Truong NP, Whittaker MR, Mak CW, Davis TP. The importance of nanoparticle shape in cancer drug delivery. Expert Opin Drug Deliv 2015;12:129–42. https://doi.org/10.1517/17425247.2014.950564.

[20]   Cheng Y, Koh LD, Li D, Ji B, Han MY, Zhang YW. On the strength of β-sheet crystallites of Bombyx mori silk fibroin. J R Soc Interface 2014;11. https://doi.org/10.1098/rsif.2014.0305.

[21]   Xi Y, Bermingham M, Wang G, Dargusch M. SPH/FE modeling of cutting force and chip formation during thermally assisted machining of Ti6Al4V alloy. Comput Mater Sci 2014;84:188–97. https://doi.org/10.1016/j.commatsci.2013.12.018.

[22]   Lucca DA, Rhorer RL, Komanduri R. Energy Dissipation in the Ultraprecision Machining of Copper. CIRP Ann - Manuf Technol 1991;40:69–72. https://doi.org/10.1016/S0007-8506(07)61936-2.

[23]   Furukawa Y, Moronuki N. Effect of Material Properties on Ultra Precise Cutting Processes. CIRP Ann - Manuf Technol 1988;37:113–6. https://doi.org/10.1016/S0007-8506(07)61598-4.

[24]   Gubbels GPH. Diamond turning of glassy polymers. 2006. https://doi.org/10.6100/IR613637.

[25]   Sima M, Özel T. Modified material constitutive models for serrated chip formation simulations and experimental validation in machining of titanium alloy Ti-6Al-4V. Int J Mach Tools Manuf 2010;50:943–60. https://doi.org/10.1016/j.ijmachtools.2010.08.004.

[26]   Wang Z, Cai Y, Luo X. Modelling and Simulation of Cutting Process by Smoothed
        Particle Hydrodynamics (SPH): A Review. 2019 25th Int. Conf. Autom. Comput.,
        IEEE; 2019, p. 1–6. https://doi.org/10.23919/IConAC.2019.8895239.

[27]   Limido J, Espinosa C, Salaün M, Lacome JL. SPH method applied to high speed
        cutting modelling. Int J Mech Sci 2007;49:898–908.
        https://doi.org/10.1016/j.ijmecsci.2006.11.005.

[28]   Bil H, Kiliç SE, Tekkaya AE. A comparison of orthogonal cutting data from
        experiments with three different finite element models. Int J Mach Tools Manuf
        2004;44:933–44. https://doi.org/10.1016/j.ijmachtools.2004.01.016.

[29]   Hallquist JO. LS-DYNA Theory Manual. Livermore Software Technology
        corporation; 2006.

[30]   Limido J, Espinosa C, Salaun M, Mabru C, Chieragatti R, Lacome JL. Metal cutting
        modelling SPH approach. Int J Mach Mach Mater 2011;9:177.
        https://doi.org/10.1504/IJMMM.2011.039645.

[31]   Zhang S, Zhang H, Zong W. Modeling and simulation on the effect of tool rake angle
        in diamond turning of KDP crystal. J Mater Process Technol 2019;273:116259.
        https://doi.org/10.1016/j.jmatprotec.2019.116259.

[32]   Abolfazl Zahedi S, Demiral M, Roy A, Silberschmidt V V. FE/SPH modelling of
        orthogonal micro-machining of f.c.c. single crystal. Comput Mater Sci 2013;78:104–9.
        https://doi.org/10.1016/j.commatsci.2013.05.022.

[33]   Umer U, Qudeiri JA, Ashfaq M, AL-Ahmari A. Chip morphology predictions while
        machining hardened tool steel using finite element and smoothed particles
        hydrodynamics methods. J Zhejiang Univ A 2016;17:873–85.
        https://doi.org/10.1631/jzus.A1600023.

[34]   Tang Z, Liu FJ, Guo SH, Chang J, Zhang JJ. Evaluation of coupled finite
        element/meshfree method for a robust full-scale crashworthiness simulation of railway
        vehicles. Adv Mech Eng 2016;8:1–13. https://doi.org/10.1177/1687814016642954.

[35] Zhu BL, Guo YL, Zhou P, Bradford MA, Pi YL. Numerical and experimental studies of corrugated-web-connected buckling-restrained braces. Eng Struct 2017;134:107–24. https://doi.org/10.1016/j.engstruct.2016.12.014.

[36] Abdalla HF, Megahed MM, Younan MYA. Shakedown Limit Loads for 90 Degree Scheduled Pipe Bends Subjected to Steady Internal Pressure and Cyclic Bending Moments. J Press Vessel Technol 2011;133. https://doi.org/10.1115/1.4002055.

[37] Takaffoli M, Papini M. Material deformation and removal due to single particle impacts on ductile materials using smoothed particle hydrodynamics. Wear 2012;274–275:50–9. https://doi.org/10.1016/j.wear.2011.08.012.

[38] Fernandes MG, Fonseca EM, Jorge RN. Thermo-mechanical stresses distribution on bone drilling: Numerical and experimental procedures. Proc Inst Mech Eng Part L J Mater Des Appl 2019;233:637–46. https://doi.org/10.1177/1464420716689337.

[39] Kitagawa T, Yabuki K. Physical properties of silk fibroin/chitosan blend films. J Appl Polym Sci 2001;80:928–34. https://doi.org/10.1002/app.1172.

[40] Choi Y, Cho SY, Heo S, Jin HJ. Enhanced mechanical properties of silk fibroin-based composite plates for fractured bone healing. Fibers Polym 2013;14:266–70. https://doi.org/10.1007/s12221-013-0266-5.

[41] White RD, Gray C, Mandelup E, Amsden JJ, Kaplan DL, Omenetto FG. Rapid nano impact printing of silk biopolymer thin films. J Micromechanics Microengineering 2011;21. https://doi.org/10.1088/0960-1317/21/11/115014.

[42] Lee WB, Wang H, Chan CY, To S. Finite element modelling of shear angle and cutting force variation induced by material anisotropy in ultra-precision diamond turning. Int J Mach Tools Manuf 2013;75:82–6. https://doi.org/10.1016/j.ijmachtools.2013.09.007.

[43] Fragassa C, Topalovic M, Pavlovic A, Vulovic S. Dealing with the effect of air in fluid structure interaction by coupled SPH-FEM methods. Materials (Basel) 2019;12. https://doi.org/10.3390/ma12071162.

[44]   Choung J, Nam W, Lee JY. Dynamic hardening behaviors of various marine structural steels considering dependencies on strain rate and temperature. Mar Struct 2013;32:49–67. https://doi.org/10.1016/j.marstruc.2013.02.001.

[45]   Lu Y, Liu K, Wang Z, Tang W. Dynamic behavior of scaled tubular K-joints subjected to impact loads. Mar Struct 2020;69:102685. https://doi.org/10.1016/j.marstruc.2019.102685.

[46]   Yang H, Yang X, Varma AH, Zhu Y. Strain-Rate Effect and Constitutive Models for Q550 High-Strength Structural Steel. J Mater Eng Perform 2019;28:6626–37. https://doi.org/10.1007/s11665-019-04431-2.

[47]   Keten S, Buehler MJ. Geometric confinement governs the rupture strength of h-bond assemblies at a critical length scale. Nano Lett 2008;8:743–8. https://doi.org/10.1021/nl0731670.

[48]   Keten S, Bertaud J, Sen D, Xu Z, Ackbarow T, Buehler MJ. Multiscale Modeling of Biological Protein Materials – Deformation and Failure, 2010, p. 473–533. https://doi.org/10.1007/978-1-4020-9785-0_17.

[49]   Keten S, Xu Z, Ihle B, Buehler MJ. Nanoconfinement controls stiffness, strength and mechanical toughness of B-sheet crystals in silk. Nat Mater 2010;9:359–67. https://doi.org/10.1038/nmat2704.

[50]   Krasnov I, Diddens I, Hauptmann N, Helms G, Ogurreck M, Seydel T, et al. Mechanical properties of silk: Interplay of deformation on macroscopic and molecular length scales. Phys Rev Lett 2008;100:2–5. https://doi.org/10.1103/PhysRevLett.100.048104.